Biomedicine & Pharmacotherapy 168 (2023) 115697

Contents lists available at ScienceDirect

Biomedicine & Pharmacotherapy

journal homepage: www.elsevier.com/locate/biopha

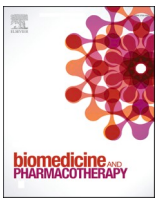

Cilostazol promotes blood vessel formation and bone regeneration in a murine non-union model

Maximilian M. Menger [a,b,*], Michelle Bleimehl [b], David Bauer [b], Claudia Scheuer [b], Sandra Hans [b], Dominik Saul [a], Sabrina Ehnert [c], Michael D. Menger [b], Tina Histing [a], Matthias W. Laschke [b]

[a] Department of Trauma and Reconstructive Surgery, Eberhard Karls University Tuebingen, BG Trauma Center Tuebingen, 72076 Tuebingen, Germany
[b] Institute for Clinical and Experimental Surgery, Saarland University, 66421 Homburg, Saar, Germany
[c] Department of Trauma and Reconstructive Surgery, BG Trauma Center Tuebingen, Siegfried Weller Institute for Trauma Research, Eberhard Karls University Tuebingen, 72076 Tuebingen, Germany

ARTICLE INFO

Keywords:
Non-union
Cilostazol
Segmental defect
Bone regeneration
Fracture healing
Angiogenesis
Mice

ABSTRACT

Non-unions represent a major complication in trauma and orthopedic surgery. Many factors contribute to bone regeneration, out of which an adequate vascularization has been recognized as crucial. The phosphodiesterase-3 (PDE-3) inhibitor cilostazol has been shown to exert pro-angiogenic and pro-osteogenic effects in a variety of preclinical studies. Hence, we herein investigated the effects of cilostazol on bone regeneration in an atrophic non-union model in mice. For this purpose, a 1.8 mm femoral segmental defect was stabilized by pin-clip fixation and the animals were treated daily with 30 mg/kg body weight cilostazol or saline (control) per os. At 2, 5 and 10 weeks after surgery the healing of femora was analyzed by X-ray, biomechanics, photoacoustic imaging, and micro-computed tomography (μCT). To investigate the cellular composition and the growth factor expression of the callus tissue additional histological, immunohistochemical and Western blot analyses were performed. Cilostazol-treated animals showed increased bone formation within the callus, resulting in an enhanced bending stiffness when compared to controls. This was associated with a more pronounced expression of vascular endothelial growth factor (VEGF), a higher number of CD31-positive microvessels and an increased oxygen saturation within the callus tissue. Furthermore, cilostazol induced higher numbers of tartrate-resistant acidic phosphate (TRAP)-positive osteoclasts and CD68-positive macrophages. Taken together, these findings demonstrate that cilostazol is a promising drug candidate for the adjuvant treatment of atrophic non-unions in clinical practice.

1. Introduction

Non-union formation is a major complication in trauma and orthopedic surgery. Despite continuously increasing knowledge about the pathophysiology of failed fracture healing, the clinical failure rate of bone healing is still up to 10% [1]. In particular, large segmental bone defects resulting from high-energy trauma, infections and tumors are associated with a high rate of non-union formation [2].

Multiple factors may affect the complex process of bone regeneration. Among these factors, a proper vascularization has been recognized as one of the major prerequisites for successful bone healing [3]. Atrophic non-unions, on the other hand, are considered to be the result of an avascular and biologically inert environment within the callus tissue [4,5]. This idea is supported by experimental studies, which demonstrate that the blockade of angiogenesis inhibits bone regeneration and results in failed fracture healing [6–8].

The phosphodiesterase-3 (PDE-3) inhibitor cilostazol elevates the cyclic adenosine monophosphate (cAMP) level, which induces blood vessel dilation and inhibits platelet aggregation [9,10]. Moreover, several studies have demonstrated in different ischemic animal models that cilostazol improves tissue perfusion and survival [11,12]. Interestingly, cilostazol promotes angiogenesis and vascularization by upregulating pro-angiogenic growth factors, such as vascular endothelial growth factor (VEGF), and exerts protective effects on endothelial cells

* Corresponding author at: Department of Trauma and Reconstructive Surgery, Eberhard Karls University Tuebingen, BG Trauma Center Tuebingen, 72076 Tuebingen, Germany.
E-mail address: mmenger@bgu-tuebingen.de (M.M. Menger).

https://doi.org/10.1016/j.biopha.2023.115697
Received 2 July 2023; Received in revised form 6 October 2023; Accepted 9 October 2023
Available online 19 October 2023

and vascular smooth muscle cells in preclinical models of hindlimb ischemia [13–16]. Notably, various experimental studies indicate that the stimulation of angiogenesis results in an accelerated fracture healing and bone regeneration [3,17]. For instance, Peng et al. [18] demonstrated in a mouse model of skull defect healing that the stimulation of angiogenesis by VEGF increases bone morphogenetic protein (BMP)− 2 induced bone formation. In addition, PDE inhibitors have been shown to stimulate the proliferation and differentiation of osteoblasts [19,20]. In line with this, we have demonstrated in a previous study that cilostazol is capable of accelerating fracture healing in a stable closed femoral fracture model in mice [21].

However, it is not known whether cilostazol is also capable of stimulating angiogenesis and bone formation in atrophic non-unions. Therefore, we herein assessed for the first time the effects of cilostazol in an atrophic non-union model in mice by X-ray, biomechanics, photoacoustic imaging, micro-computed tomography (μCT) as well as histological, immunohistochemical and Western blot analyses.

2. Materials and methods

2.1. Animals

All animal experiments were approved by the local governmental animal protection committee (permit number: 13/2019). The study was executed according to the European legislation on the protection of animals (Directive 2010/63/EU) and the National Institutes of Health (NIH) Guide for the Care and Use of Laboratory Animals (Institute of Laboratory Animal Resources, National Research Council, Washington DC, USA).

A total number of 58 CD-1 mice with an age of 12–16 weeks and a body weight of 30–40 g were used. Notably, the age of 12–16 weeks corresponds to the age of young adult mice [22]. The animals were bred at the Institute for Clinical and Experimental Surgery, Saarland University, Germany, and housed at a regular 12 h/12 h light and dark cycle with free access to tap water and standard pellet food (Altromin, Lage, Germany).

2.2. Surgical procedure

Mice were anesthetized by an intraperitoneal (i.p.) injection of ketamine (75 mg/kg body weight; Ursotamin®, Serumwerke Bernburg, Bernburg, Germany) and xylazine (15 mg/kg body weight; Rompun®, Bayer, Leverkusen, Germany). To evaluate the effects of cilostazol on bone regeneration, we used a well-established murine non-union model, as introduced by Garcia et al. [23].

All procedures were performed under aseptic conditions using an operating microscope to achieve an adequate precision. After a ~4 mm medial parapatellar incision at the right knee, the patella was dislocated laterally. A hole with a diameter of 0.5 mm was drilled into the intracondylar notch and a distally flattened press fit 24 Gauge needle with a diameter of 0.55 mm was implanted intramedullary before the wound was closed. The pin was flattened at the distal end to avoid secondary dislocation. Afterwards, the diaphysis of the femur was exposed by a lateral approach. Subsequently, a custom-made clip of 6 mm length was implanted ventrodorsally into the femur and lateral of the already implanted pin. A gap size of 1.8 mm was created by means of a spherical trephine under permanent saline solution cooling. Furthermore, the periosteum was stripped 2 mm proximally and distally of the gap along the longitudinal axis of the femoral bone. The implant position was confirmed by radiography (MX-20, Faxitron X-ray Corporation, Wheelin, IL, USA). For analgesia, the mice received tramadol-hydrochloride (Grünenthal, Aachen, Germany) in the drinking water (1 mg/mL) one day prior to surgery until three days after surgery.

Twenty-nine mice were treated daily with 30 mg/kg body weight cilostazol (Pletal®, Otsuka, Wexham, UK; dissolved in 100 μL saline) per os (p.o.) by gavage. Control mice (n = 29) received equal amounts of saline. At 2 weeks (n = 9 each group; 5 male and 4 female each group), 5 weeks (n = 8 each group; 5 male and 3 female each group) and 10 weeks (n = 9; 7 male and 2 female each group) the animals were sacrificed by an overdose of anesthetics and the femora were excised for further radiological and histological analyses. Additional animals were sacrificed accordingly at 2 weeks (n = 3 each group; 1 male and 2 female each group) for Western blot analyses of the callus tissue.

2.3. X-ray analysis

The femora were analyzed to conform adequate implant position and signs of osseous bridging at 2, 5 and 10 weeks after surgery. For this purpose, the animals were anesthetized again and lateral radiographs of the osteotomized femora were performed.

2.4. Biomechanics

After removal of the soft tissue and the implants, the bending stiffness of the femora was measured by a 3-point-bending device using a non-destructive approach. This allowed for the subsequent use of the specimens for additional μCT, histology and immunohistochemistry and, hence, a marked reduction of the number of required laboratory animals according to the 3 R principle. To guarantee standardized measuring conditions, femora were always mounted with the ventral aspect upwards. Due to the different stages of healing, the loads, which had to be applied, varied markedly between the individual animals and time points. Hence, loading was stopped individually in every case when the actual load-displacement curve deviated more than 1% from linearity. Bending stiffness (N/mm) was calculated from the linear elastic part of the load-displacement diagram [24].

2.5. Ultrasound and photoacoustic imaging

Ultrasound and photoacoustic imaging was performed at 2, 5 and 10 weeks after surgery by means of a Vevo LAZR system (FUJIFILM VisualSonics Inc.; Toronto, ON, Canada) and a real-time micro-visualization LZ550 linear-array transducer (FUJIFILM VisualSonics Inc.) with a center frequency of 40 MHz. For this purpose, the animals were anesthetized with 1.5% isoflurane and subsequently fixed in prone position on a heated stage. The skin was shaved dorsally around the right thigh and sterile ultrasound gel was applied to avoid air interference with ultrasound coupling into the animal. Additionally, a compress was positioned underneath the right hind limb to avoid artefact signals from the heated stage. During the photoacoustic imaging, the heart rate and respiratory rate were constantly monitored, and the body temperature was maintained at 36–37 °C (THM100; Indus Instruments, Houston, TX, USA) to guarantee an adequate standardization.

For three-dimensional, high-resolution B-mode ultrasound and OxyHemo-mode photoacoustic image acquisition, the scan head was driven by a linear motor to acquire two-dimensional parallel images at regular spatial intervals of 50 μm over the entire femur. A pulsed laser induced a thermoelastic expansion at the extinction wavelength of 750 nm for Hb and at 850 nm for HbO_2. The resulting acoustic emissions were detected by a transducer. OxyHemo-mode photoacoustic images were recorded at 750 nm and 850 nm with a two-dimensional gain of 42 dB. To measure the total hemoglobin (HbT)/volume ($1/mm^3$) within the callus tissue, all detected signals at the two wavelengths were divided by the volume of the callus [25]. Furthermore, oxygen saturation (sO_2, %) within the callus tissue of unions and non-unions was evaluated, as previously described [26–29]. All values were computed using the Vevo LAB 1.7.2. software (FUJIFILM VisualSonics Inc.).

μCT.

The femora were scanned (Skyscan 1172, Bruker, Billerica, MA) at a spatial resolution of 6.5 μm with a standardized setup (tube voltage: 50 kV; current: 200 μA; intervals: 0.4°; exposure time: 3500 ms; filter: 0.5 mm aluminum). Images were stored in three-dimensional arrays. To

express gray values as mineral content (bone mineral density; BMD), calcium hydroxyapatite (CaHA) phantom rods with known BMD values (0.250 g and 0.750 g CaHA/ cm^3) were employed for calibration. The region of interest (ROI) defining the callus tissue was contoured manually excluding any original cortical bone. Thresholding allowed the differentiation between poorly and highly mineralized bone. The thresholds to distinguish between poorly and highly mineralized bone were based upon visual inspection of the images, qualitative comparison with histological sections and other studies investigating bone repair and callus tissue by μCT [30,31]. A BMD with more than 0.642 g/cm^3, resulting in gray values of 98–255, was defined as highly mineralized bone. Poorly mineralized bone was assumed to have a BMD value between 0.410 g/cm^3 and 0.642 g/cm^3, resulting in gray values of 68–97.

The following parameters were calculated from the callus region of interest for each specimen: poorly mineralized bone volume (BV_{low}), highly mineralized bone volume (BV_{high}), bone volume fraction of tissue volume (BV/TV), trabecular thickness, trabecular separation and trabecular number.

2.6. Histology and histomorphometry

For further histological analyses, bones were fixed in paraformaldehyde for 24 h. Subsequently, the specimens were embedded in a 30% sucrose solution for another 24 h and then frozen at − 80 °C. Longitudinal sections through the femoral axis with a thickness of 4 μm were cut by the Kawamotos film method for histomorphometric analyses and stained with Safranin-O. At a magnification of 12.5x (Olympus BX60 Microscope, Olympus, Shinjuku, Japan; Zeiss Axio Cam and Axio Vision 3.1, Zeiss, Oberkochen, Germany) structural indices were calculated according to the recommendations of Gerstenfeld et al. [32]. The following histomorphometric parameters of the bone defects were evaluated: (i) total callus area; (ii) ratio of bone callus area; (iii) ratio of cartilaginous callus area and (iv) ratio of fibrous callus area. The total callus area was defined as the entire osseous, cartilaginous and fibrous callus tissue between the two drilling holes. Pre-existing cortical bone of the proximal and distal fragment was excluded. To mark and calculate each area the ImageJ analysis system (NIH, Bethesda, USA) was used.

In addition, tartrate-resistant acid phosphate (TRAP) activity was analyzed in the callus tissue at 2, 5 and 10 weeks after surgery. For this purpose, longitudinal sections of 4 μm were incubated in a mixture of 5 mg naphthol AS-MX phosphate and 11 mg fast red TR salt in 10 mL 0.2 M sodium acetate buffer (pH 5.0) for 1 h at 37 °C. Sections were counterstained with methyl green and covered with glycerin gelatin. In the specimens, one high-power field (HPF, 400x magnification) was placed in a standardized manner in the central interfragmentary region of the callus, while three additional HPFs were placed on each site of the periosteal callus. TRAP-positive osteoclasts (three or more nuclei each cell) were counted in each HPF, and the mean of each specimen was determined.

2.7. Immunohistochemistry

To further investigate the cellular composition within the callus tissue at 2, 5 and 10 weeks after surgery, longitudinal sections with a thickness of 4 μm were cut. For the immunohistochemical detection of microvessels, sections were stained with a monoclonal rat anti-mouse antibody against the endothelial cell marker CD31 (1:100; Abcam, Cambridge, UK). A goat anti-rat IgG-Alexa555 antibody served as secondary antibody (1:100; Life Technology, Eugene, USA). Cell nuclei were stained with Hoechst 33342 (2 μg/mL; Sigma-Aldrich, Taufkirchen Germany). To detect the macrophage marker CD68, sections were stained with a polyclonal rabbit anti-mouse antibody against CD68 (1:100; Abcam). A goat anti-rabbit IgG-antibody (1:200; Dianova, Hamburg, Germany) served as corresponding secondary antibody.

In the specimens, one HPF was placed in a standardized manner in the central interfragmentary region of the callus, while three additional HPFs were placed on each site of the periosteal callus. The number of CD31-positive microvessels and CD68-positive cells were counted in each HPF and the mean of each specimen was determined.

2.8. Western blot

Protein expression within the callus tissue was determined by Western blot analysis, including the expression of VEGF, receptor activator of NF-κB ligand (RANKL) and osteoprotegerin (OPG). The callus tissue was frozen and stored at − 80 °C until required. Analyses were performed of the callus tissue at 2 weeks after surgery (n = 3 per group). After saving the whole protein fraction, the analyses were performed using rabbit anti-mouse VEGF (1:300, Abcam) rabbit anti-mouse RANKL (1:300, Abcam) and rabbit anti-mouse OPG (1:300, Biozol Diagnostica, Eching, Germany) antibodies. Primary antibodies were followed by corresponding horseradish peroxidase-conjugated secondary antibodies (1:1000, Dako Deutschland GmbH (Agilent), Hamburg, Germany). Protein expression was visualized by means of luminol-enhanced chemiluminescence after exposure of the memsbrane to the Intas ECL Chemocam Imager (Intas Science Imaging Instrument GmbH, Göttingen, Germany) and normalized to β-actin signals (1:1000, mouse anti-mouse β-actin, Santa Cruz Biotechnology, Heidelberg, Germany) to correct for unequal loading.

2.9. Statistical analysis

All data are given as means ± standard error of the mean (SEM). After testing the data for normal distribution (Kolmogorov-Smirnov test) and equal variance (*F*-test), comparisons between the two groups were performed by the unpaired Student's *t*-test. For non-parametrical data, a Mann-Whitney *U*-test was used. All statistics were performed using the SigmaPlot 13.0 software (Jandel Corporation, San Rafael, CA, USA). A p-value of < 0.05 was considered to indicate significant differences.

3. Results

3.1. X-ray analysis

The X-rays taken prior to sacrificing the animals showed no implant dislocation at 2, 5 or 10 weeks after surgery in both study groups. As expected, at 10 weeks after surgery the femora of control animals exhibited no signs of osseous bridging with a persisting gap between the rounded adjoining bone fragments, indicating atrophic non-union formation (Fig. 1a). In cilostazol-treated animals, on the other hand, clear radiological signs of callus formation could be observed at 10 weeks after surgery within the osteotomy gap (Fig. 1b).

3.2. Biomechanics

The biomechanical analysis revealed a significantly higher bending stiffness at 10 weeks after surgery in cilostazol-treated animals when compared to controls (Fig. 1c). Notably, the bending stiffness in control mice remained < 1 N/mm, indicating non-union formation. At 2 and 5 weeks after surgery the bending stiffness did not significantly differ between the two study groups.

3.3. Ultrasound and photoacoustic imaging

Controls and cilostazol-treated animals were investigated 2 (Figs. 2a-f), 5 (Fig. 2g-l) and 10 weeks (Fig. 2m-r) after surgery by ultrasound and photoacoustic imaging. Ultrasound imaging enabled a clear and reliable visualization of the mouse femur. In control animals, the ultrasound imaging showed a persisting osteotomy gap throughout the entire observation period (Fig. 2a, g, m), whereas some callus formation was visible in cilostazol-treated mice at 10 weeks after surgery (Fig. 2p). At 2 weeks after surgery the photoacoustic analysis did not show any

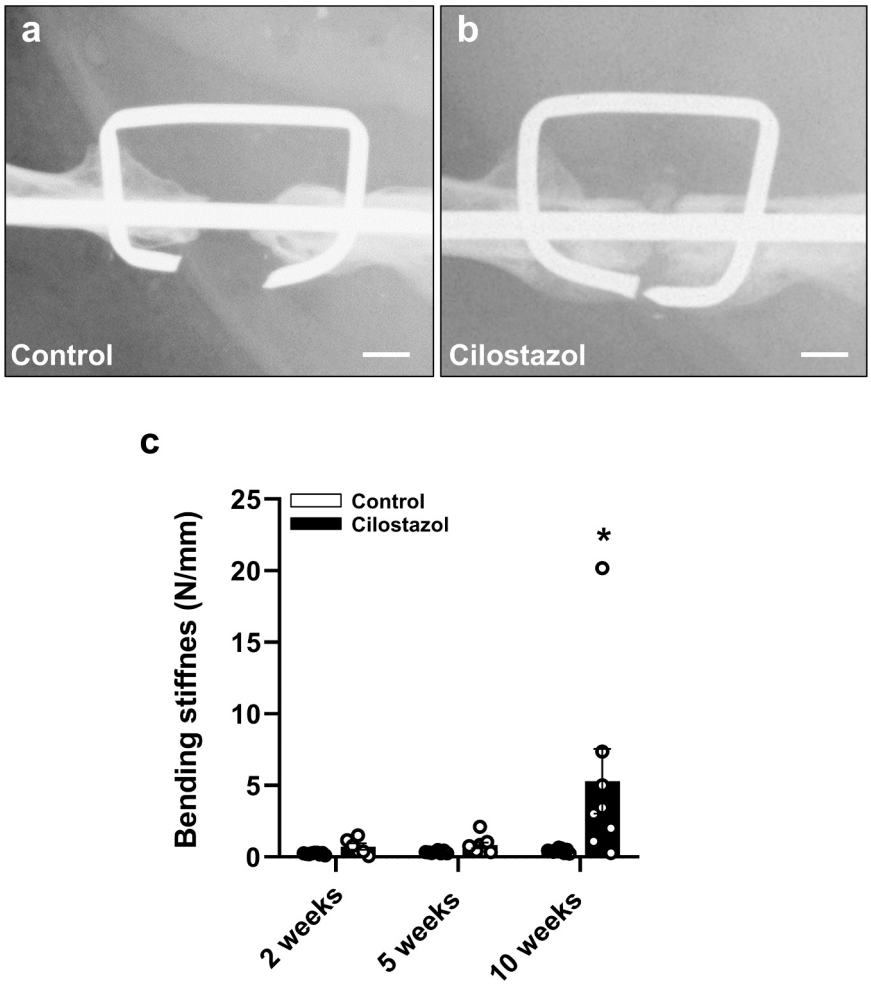

Fig. 1. (a, b) Representative X-rays of the femur of a control (a) and a cilostazol-treated mouse (b) 10 weeks after surgery. Scale bars: 1 mm. (c) Bending stiffness (N/mm) of controls (white bars, n = 9 at 2 (5 male; 4 female) and 10 weeks (7 male; 2 female) n = 8 at 5 weeks (5 male; 3 female)) and cilostazol-treated animals (black bars, n = 6 at 2 weeks (3 male; 3 female), n = 8 at 5 (5 male; 3 female) and 10 weeks (6 male; 2 female)) at 2, 5 and 10 weeks after surgery. Mean ± SEM; *p < 0.05 vs. control.

difference in sO_2 within the callus tissue between the two study groups (Fig. 2 s). In contrast, we detected a significantly higher sO_2 within the callus at 5 and 10 weeks after surgery in cilostazol-treated mice when compared to controls (Fig. 2 s). Moreover, we found a statistically significant higher amount of HbT/volume, at 2 and 10 weeks after surgery. Notably, at 5 weeks the HbT/volume was only slightly increased when compared to the respective controls (Fig. 2t).

3.4. μCT

Additional radiological analyses by means of μCT demonstrated a significantly higher poorly and highly mineralized bone volume at 2 (Figs. 3a and b) and 5 weeks (Fig. 3c and d) after surgery in cilostazol-treated mice when compared to controls. At 10 weeks after surgery the amount of poorly mineralized bone tissue was slightly enhanced, and the highly mineralized bone tissue was significantly increased in cilostazol-treated animals (Fig. 3e and f). Notably, the 3D-recontructions of our μCT analyses showed a persisting fracture gap in control animals throughout the entire observation period, confirming a reliable non-union formation. In cilostazol-treated mice, signs of bone formation within the fracture gap were clearly visible (Fig. 3a, c and e).

Further μCT analyses revealed a significantly higher BV/TV in the cilostazol group at 2 and 10 weeks after surgery (Fig. 4a). At 5 weeks the results demonstrated a slight, but not significant, increase in BV/TV in cilostazol-treated animals when compared to controls (Fig. 4a). Moreover, in cilostazol-treated mice we detected a significantly larger trabecular thickness throughout the entire observation period (Fig. 4b). In addition, the trabecular number was significantly higher at 10 weeks after surgery in the cilostazol group when compared to controls (Fig. 4c). At 2 and 5 weeks after surgery the trabecular number did not significantly differ between the two study groups (Fig. 4c). The trabecular separation was significantly higher at 2 weeks, whereas at 10 weeks after surgery the analyses demonstrated a significantly lower trabecular separation in cilostazol-treated mice (Fig. 4d). At 5 weeks after surgery the μCT analyses demonstrated no differences in trabecular separation between the two study groups (Fig. 4d).

3.5. Histomorphometric and histological analysis

The histomorphometric analyses confirmed the findings of our radiological analysis, demonstrating in control animals a persisting fracture gap filled with abundant fibrous tissue between adjoining bone fragments at 10 weeks after surgery (Fig. 5a). In cilostazol-treated mice, clear signs of novel bone formation were visible; however, a complete osseous bridging was absent (Fig. 5b). Quantitative analyses showed a larger fracture callus in cilostazol-treated mice at 2, 5 and 10 weeks after surgery when compared to controls (Fig. 5c, d and e). At 2 (Fig. 5 f) and 5 weeks (Fig. 5 g) after surgery the callus composition did not significantly differ between the two study groups. However, at 10 weeks after surgery our analysis showed a significantly higher ratio of bone tissue

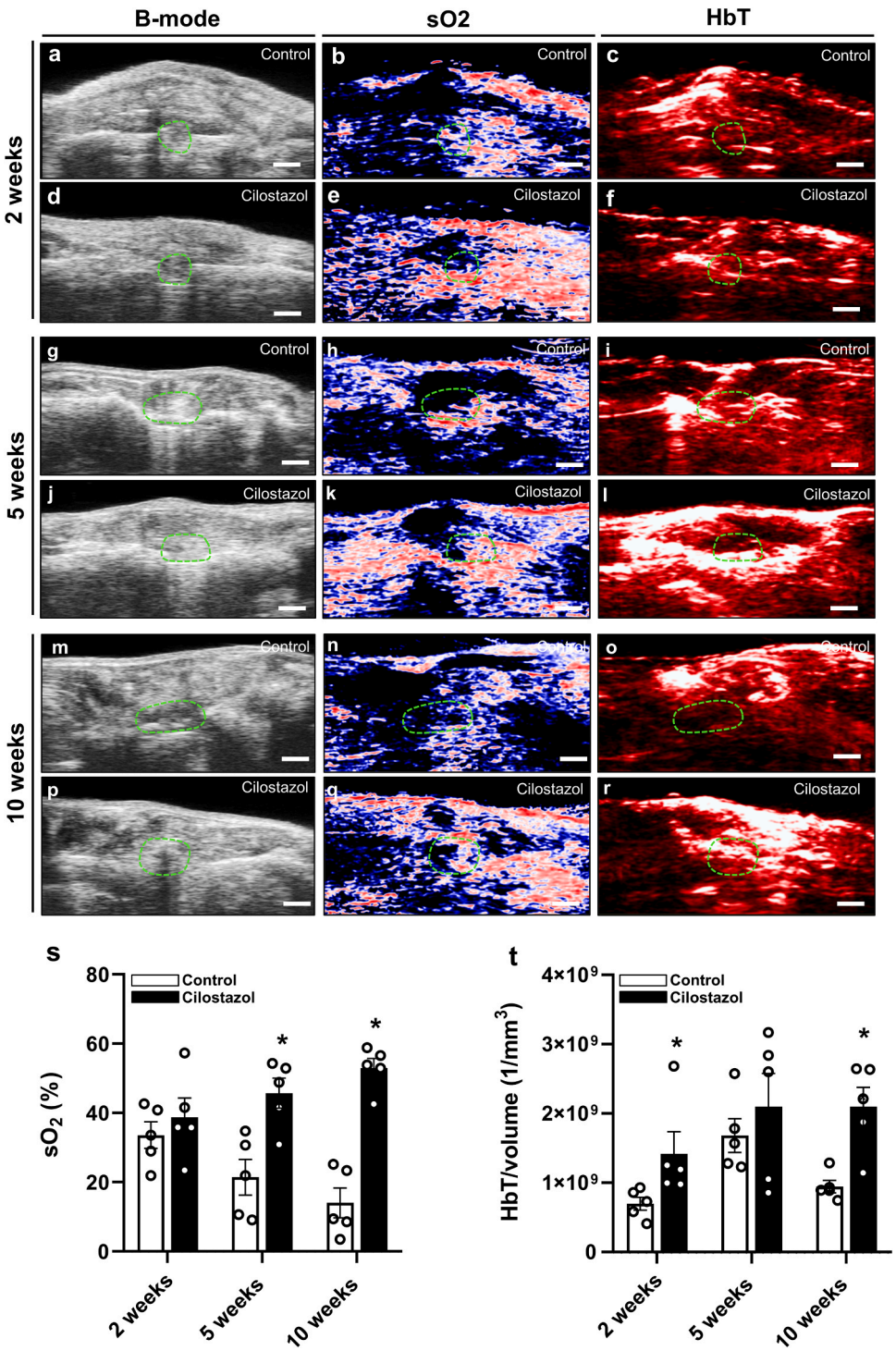

Fig. 2. (a-r) Representative images of B-mode, hemoglobin oxygen saturation (sO_2) and total hemoglobin (HbT) in controls and cilostazol-treated animals at 2 (a-f), 5 (g-l) and 10 weeks (m-r) after surgery. The callus tissue is marked by green broken lines. Scale bars: 1.5 mm. (s) sO_2 (%) within the callus tissue of controls (white bars, n = 5 at 2, 5 and 10 weeks (3 male; 2 female)) and cilostazol-treated animals (black bars, n = 5 at 2, 5 and 10 weeks (3 male; 2 female)). Mean ± SEM; *p < 0.05 vs. control. (t) HbT/volume (1/mm^3) within the callus tissue of controls (white bars, n = 5 at 2, 5 and 10 weeks (3 male; 2 female)) and cilostazol-treated animals (black bars, n = 5 at 2, 5 and 10 weeks (3 male; 2 female)). Mean ± SEM; *p < 0.05 vs. control.

and a significantly lower amount of fibrous tissue within the callus of cilostazol-treated animals (Fig. 5 h). In contrast, the ratio of cartilaginous tissue did not significantly differ between the cilostazol and the control group (Fig. 5 h).

Additional histological analyses revealed at 2 weeks after surgery a slightly higher number of TRAP-positive osteoclasts within the callus tissue of cilostazol-treated mice (Fig. 6a, b and c), and at 5 and 10 weeks after surgery a significantly higher number when compared to respective controls (Fig. 6a, b and c).

3.6. Immunohistochemical analysis

In order to analyze the vascularization and immunogenic response within the callus tissue, we performed additional immunohistochemical

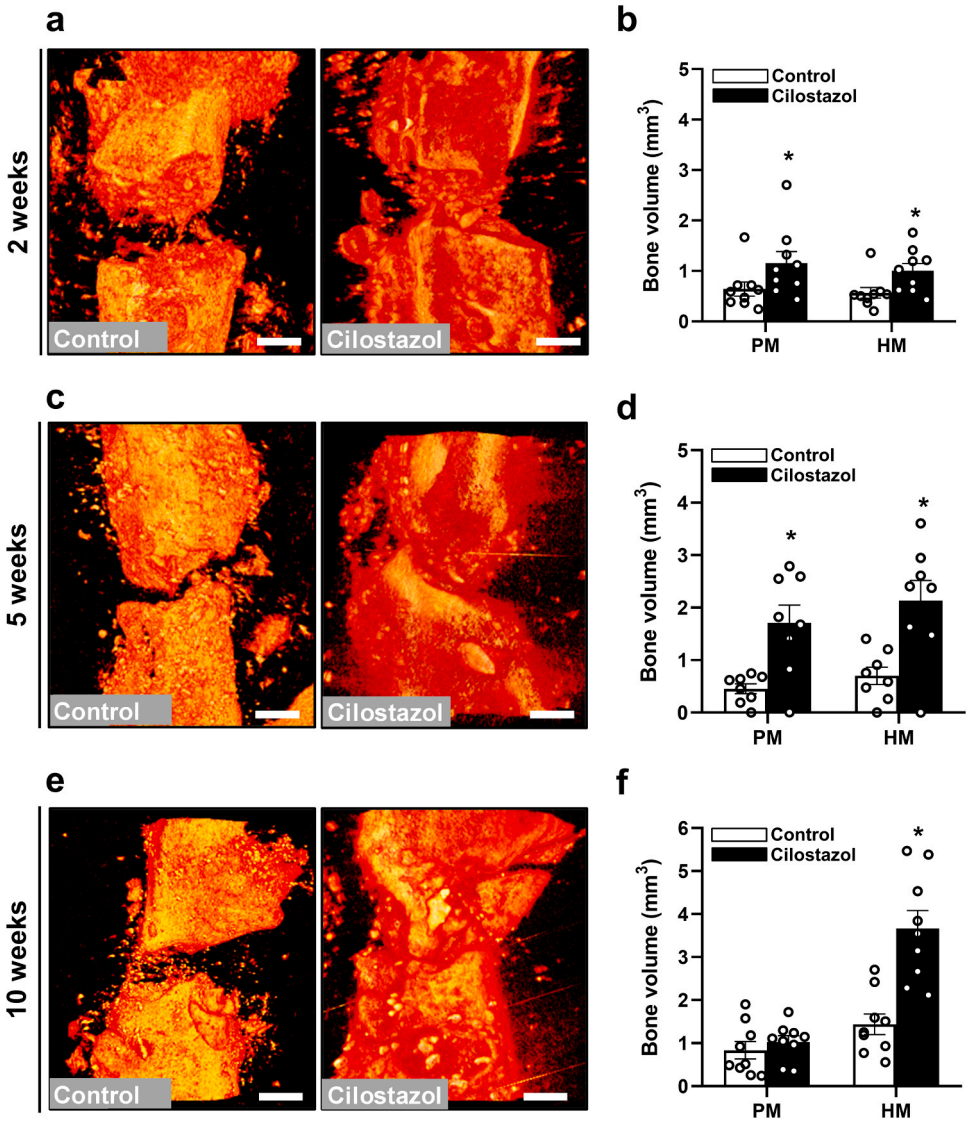

Fig. 3. (a, c, e) Representative μCT-3D reconstructions of femora in controls and cilostazol-treated mice at 2 (a), 5 (c) and 10 weeks (e) after surgery. Scale bars: 0.5 mm. (b, d, f) Poorly (PM) and highly (HM) mineralized bone volume (mm^3) of the callus tissue of controls (white bars, n = 9 at 2 (5 male; 4 female) and 10 weeks (7 male; 2 female), n = 8 at 5 weeks (5 male; 3 female)) and cilostazol-treated mice (black bars, n = 9 at 2 (5 male; 4 female) and 10 weeks (7 male; 2 female), n = 8 at 5 weeks (5 male; 3 female)) at 2 (b), 5 (d) and 10 (f) weeks after surgery. Mean ± SEM; *p < 0.05 vs. control.

analyses. Our data demonstrated a significantly higher amount of CD31-positive microvessels within the callus tissue of cilostazol-treated animals throughout the entire observation period when compared to controls (Fig. 6d, e and f). Furthermore, our analyses showed a significantly higher number of CD68-positive macrophages within the callus tissue of cilostazol-treated mice at 2 weeks after surgery (Fig. 6 g, h and i). Notably, at 5 and 10 weeks after surgery the number of CD68-positive macrophages did not significantly differ between the two study groups (Fig. 6 g, h and i). In order to validate the quality of the immunohistochemical staining, negative controls of CD31-staining (Fig. 6j) and CD68-staining (Fig. 6 k) are demonstrated.

3.7. Western blot analysis

Our Western blot analysis at 2 weeks after surgery showed a significantly higher expression of the pro-angiogenic marker VEGF within the callus tissue of cilostazol-treated mice when compared to controls (Fig. 7a and b). Moreover, the analysis revealed a nearly 3-fold higher expression of RANKL in cilostazol-treated animals (Fig. 7c and d). Additionally, the expression of OPG was more than 10-fold higher in cilostazol-treated animals when compared to controls (Fig. 7e and f). However, the increased expression of both RANKL and OPG was not found significant when compared to controls.

4. Discussion

Non-union formation is a major problem in modern trauma and orthopedic surgery. For the patient, the failed fracture healing results in significant pain and hospitalization, which is associated with multiple, often complex, and extensive revision surgeries. For the society, the emerging costs pose an immense burden to the health care system [33,34]. Treatment of non-union patients with the PDE-3 inhibitor cilostazol may help to overcome this problem due to its pro-angiogenic and pro-osteogenic effect profile [11,20]. In fact, in the present study we were able to demonstrate that cilostazol effectively stimulates bone formation in an atrophic non-union model in mice.

The non-union model by Garcia et al. [23] used in the present study results in a failure of fracture healing 10 weeks after surgery, leading to non-union formation [35]. The intramedullary pin and ventro-dorsally implanted clip provide both axial and rotational stability and, hence, a

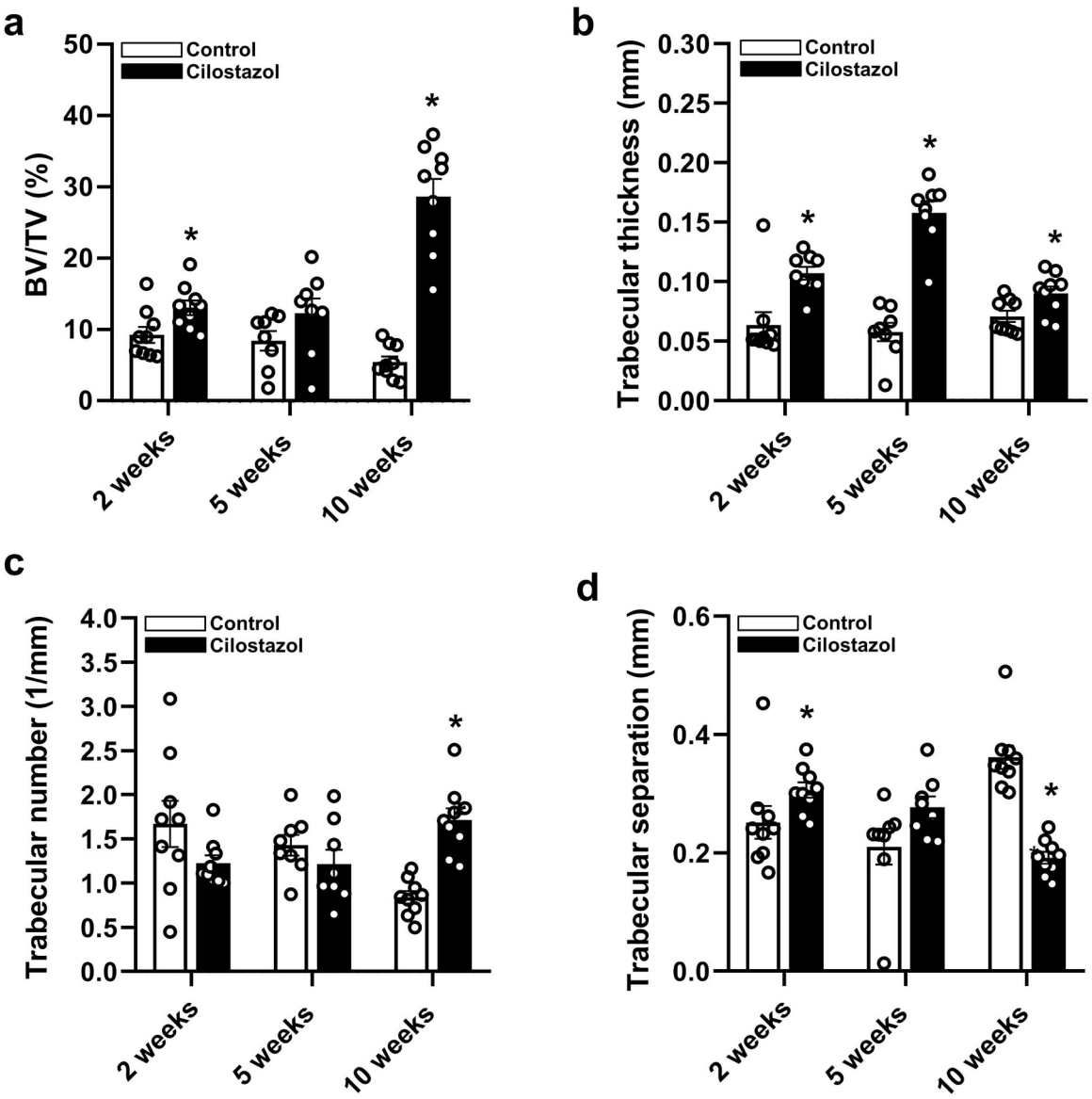

Fig. 4. (a-d) BV/TV (%) (a), trabecular thickness (mm) (b), trabecular number (1/mm) (c) and trabecular separation (mm) (d) of the callus tissue of controls (white bars, n = 9 at 2 (5 male; 4 female) and 10 weeks (7 male; 2 female), n = 8 at 5 weeks (5 male; 3 female)) and cilostazol-treated mice (black bars, n = 9 at 2 (5 male; 4 female) and 10 weeks (7 male; 2 female), n = 8 at 5 weeks (5 male; 3 female)) at 2, 5 and 10 weeks after surgery. Mean ± SEM; *p < 0.05 vs. control.

reliable osteosynthesis. Notably, the periosteal stripping is necessary to achieve a non-union rate of 100% [23]. The time points of observation were chosen at 2, 5 and 10 weeks after surgery. The analysis at 2 weeks was used for the investigation of bone regeneration at an early time point. Furthermore, this time point also served for the observation of growth factor expression. The 10 weeks analysis was chosen for the investigation of bone regeneration at a late time point, when non-union formation was fully established in the control group [22,23,35]. Additionally, the 5 weeks time point was chosen to obtain additional information on the healing process between the early and late time point of healing. Five weeks is the usual time period for successful fracture healing in mice under physiological conditions [36].

At 10 weeks after surgery the control group revealed a reliable non-union formation with abundant fibrous tissue between the adjoining bone fragments. In cilostazol-treated animals, however, the radiological and histological analyses showed a significantly higher amount of bone tissue. The progressing bone regeneration resulted in an enhanced biomechanical stiffness of mice femora at 10 weeks after surgery. These findings may be explained by the fact that we detected a significantly upregulated expression of VEGF in the callus tissue. Indeed, bone tissue is highly vascularized and healing bone crucially relies on the formation of new blood vessels and their interaction with bone cells [37]. The newly formed blood vessels provide an adequate supply of the fracture site with oxygen, nutrients and progenitor cells [38]. Hence, angiogenesis is one of the first steps that occur during the physiological sequence of endochondral and intramembranous fracture healing. Accordingly, preclinical studies demonstrate that the inhibition of angiogenesis may lead to a failure of fracture healing and eventually results in non-union formation. For instance, Hausman et al. [39] used a closed murine femoral fracture model to show that the inhibition of blood vessel formation by TNP-470 completely prevents fracture healing. In line with these results, our immunohistochemical analysis revealed that the increased bone formation in cilostazol-treated mice is associated with a higher number of CD31-positive microvessels and, thus, an increased oxygen saturation within the callus tissue.

Of interest, experimental studies demonstrated that the actions of VEGF exceed the sole stimulation of angiogenesis. This growth factor is also capable of directly stimulating endochondral and intramembranous

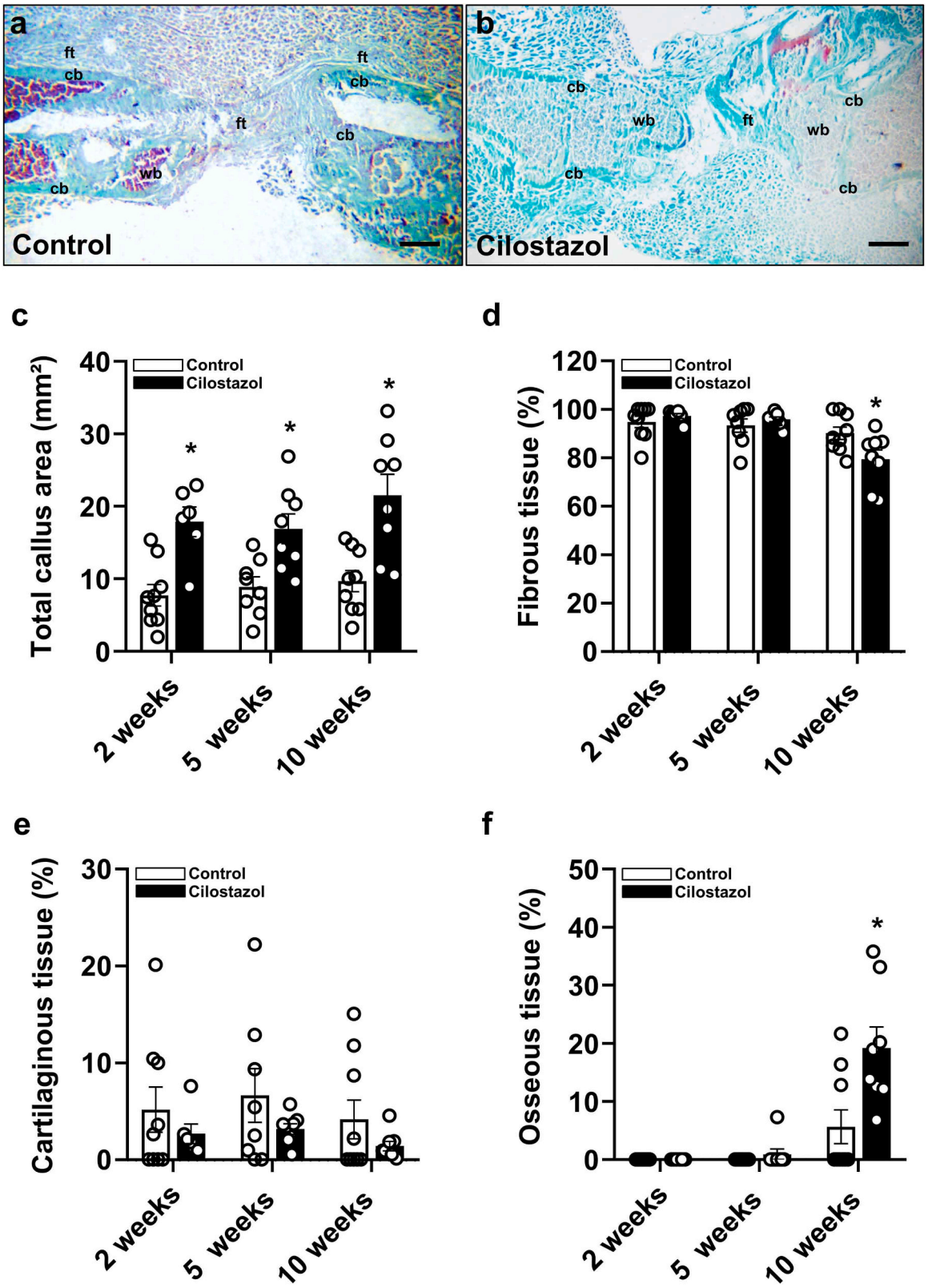

Fig. 5. (a, b) Representative histological images of the Safranin-O-stained femur in a control (a) and cilostazol-treated mouse (b) at 10 weeks after surgery. Fibrous tissue (ft), woven bone (wb) and cortical bone (cb) are indicated. Scale bars: 0.5 mm. (c-f) Total callus area (mm^2) (c), ratio of fibrous tissue (%) (d), ratio of cartilaginous tissue (%) (e) and ratio of osseous tissue (%) (f) of femora of controls (white bars, n = 9 at 2 (5 male; 4 female) and 10 weeks (7 male; 2 female), n = 8 at 5 weeks (5 male; 3 female)) and cilostazol-treated mice (black bars, n = 6 at 2 weeks (3 male; 3 female), n = 8 at 5 (5 male; 3 female) and 10 weeks (6 male; 2 female)) at 2, 5 and 10 weeks after surgery. Mean ± SEM; *$p < 0.05$ vs. control.

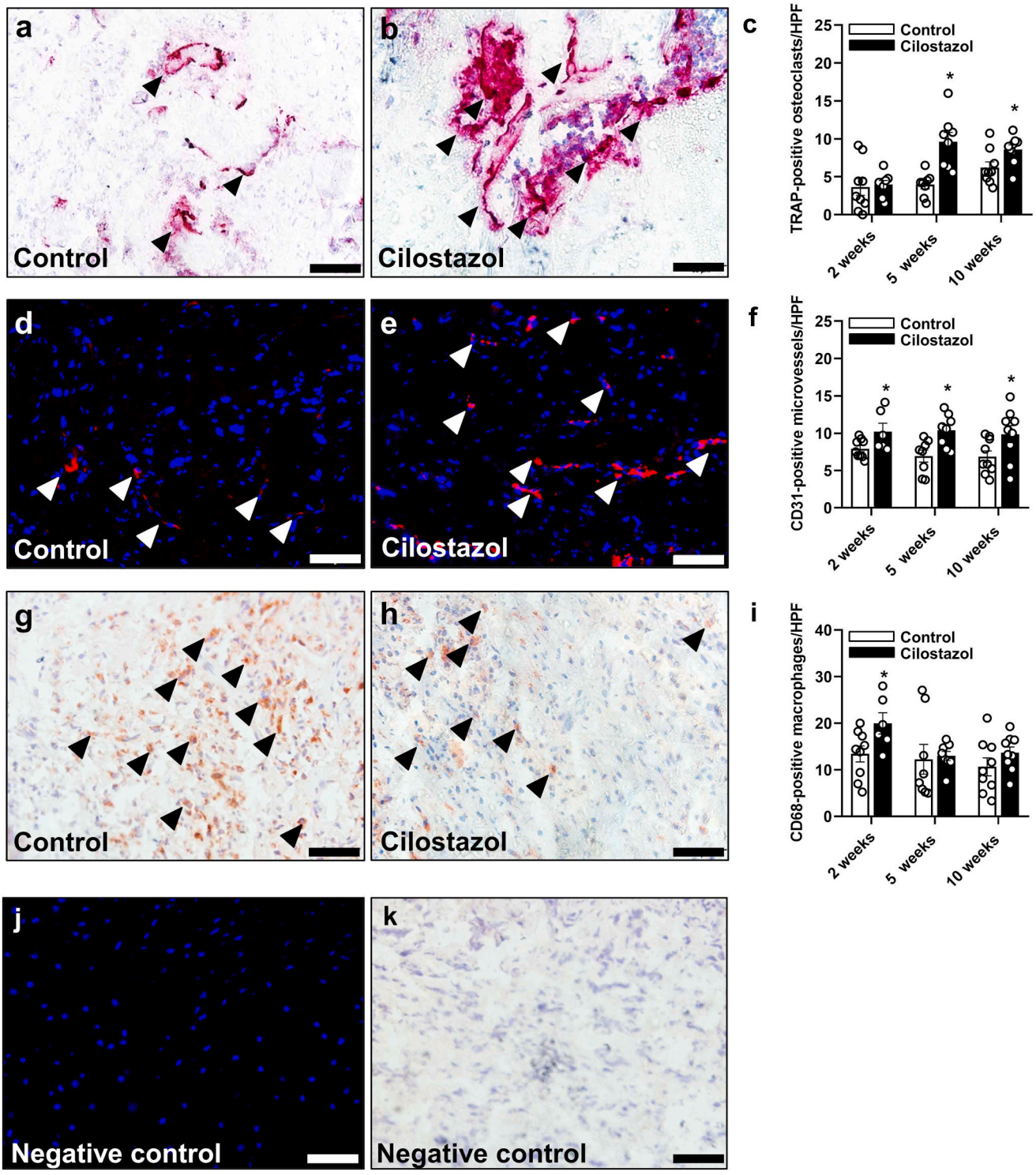

Fig. 6. (a, b) Representative histological images of TRAP-positive osteoclasts (arrowheads) within the callus tissue of a control (a) and cilostazol-treated mouse (b) at 5 weeks after surgery. Scale bars: 50 μm. (c) TRAP-positive osteoclasts/HPF within the callus tissue of controls (white bars, n = 9 at 2 (5 male; 4 female) and 10 weeks (7 male; 2 female), n = 8 at 5 weeks (5 male; 3 female)) and cilostazol-treated mice (black bars, n = 8 at 2 (5 male; 3 female) and 5 weeks (5 male; 3 female), n = 9 at 10 weeks (7 male; 2 female)) at 2, 5 and 10 weeks after surgery. Mean ± SEM; *p < 0.05 vs. control. (d, e) Representative immunohistochemical images of CD31-positive microvessels (arrowheads) within the callus tissue of a control (d) and cilostazol-treated mouse (e) at 2 weeks after surgery. Scale bars: 50 μm. (f) CD31-positive microvessels/HPF within the callus tissue of controls (white bars, n = 9 at 2 (5 male; 4 female) and 10 weeks (7 male; 2 female), n = 8 at 5 weeks (5 male; 3 female)) and cilostazol-treated mice (black bars, n = 6 at 2 weeks (3 male; 3 female), n = 8 at 5 weeks (5 male; 3 female), n = 9 at 10 weeks (7 male; 2 female)) at 2, 5 and 10 weeks after surgery. Mean ± SEM; *p < 0.05 vs. control. (g, h) Representative immunohistochemical images of CD68-positive cells (arrowheads) within the callus tissue of a control (g) and cilostazol-treated mouse (h) at 2 weeks after surgery. Scale bars: 50 μm. (i) CD68-positive cells/HPF within the callus tissue of controls white bars, n = 9 at 2 (5 male; 4 female) and 10 weeks (7 male; 2 female), n = 8 at 5 weeks (5 male; 3 female)) and cilostazol-treated mice (black bars, n = 6 at 2 (3 male; 3 female), n = 8 at 5 weeks (5 male; 3 female), n = 9 at 10 weeks (7 male; 2 female)) at 2, 5 and 10 weeks after surgery. (j, k) Negative controls of CD31- (j) and CD68-staining (k). Scale bars: 50 μm. Mean ± SEM; *p < 0.05 vs. control.

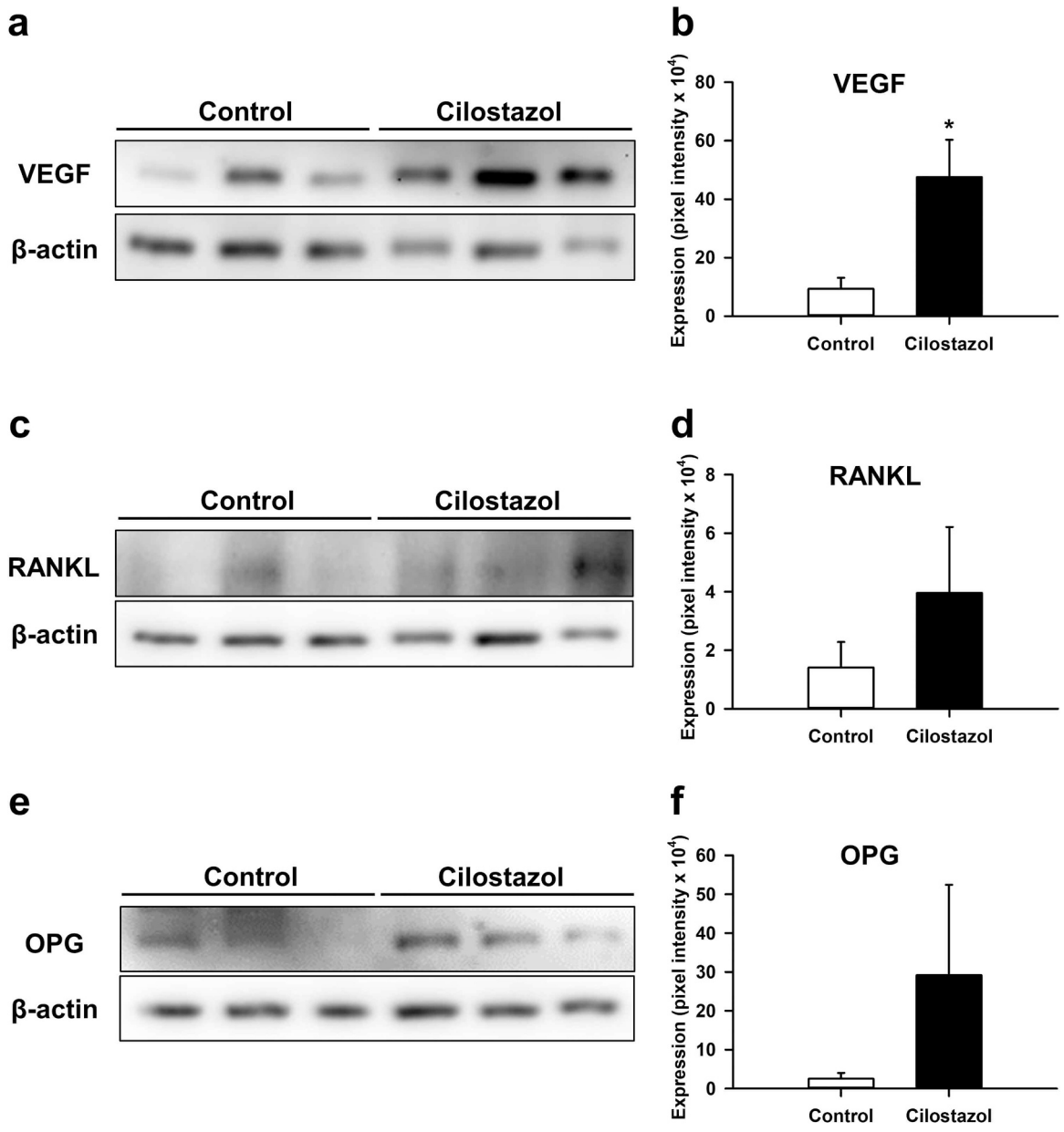

Fig. 7. **(a)** Representative Western blots of VEGF expression within the callus tissue of controls and cilostazol-treated mice at 2 weeks after surgery. **(b)** Expression of VEGF (pixel intensity x 10^4) within the callus tissue of controls (white bars, n = 3 (1 male; 2 female)) and cilostazol-treated mice (black bars, n = 3 (1 male; 2 female)) at 2 weeks after surgery. Mean ± SEM; *$p < 0.05$ vs. control. **(c)** Representative Western blots of RANKL expression within the callus tissue of controls and cilostazol-treated mice at 2 weeks after surgery. **(d)** Expression of RANKL (pixel intensity x 10^4) within the callus tissue of controls (white bars, n = 3 (1 male; 2 female)) and cilostazol-treated mice (black bars, n = 3 (1 male; 2 female)) at 2 after surgery. Mean ± SEM. **(e)** Representative Western blots of OPG expression within the callus tissue of controls and cilostazol-treated mice at 2 weeks after surgery. **(f)** Expression of OPG (pixel intensity x 10^4) within the callus tissue of controls (white bars, n = 3 (1 male; 2 female)) and cilostazol-treated mice (black bars, n = 3 (1 male; 2 female)) at 2 weeks after surgery. Mean ± SEM.

bone formation [40,41]. Therefore, the improved bone regeneration observed in cilostazol-treated mice is most likely caused by both pro-angiogenic and pro-osteogenic effects of the enhanced VEGF expression.

In addition, we analyzed the number and activity of osteoclasts. Interestingly, we detected a higher number of osteoclasts within the callus tissue of cilostazol-treated animals. This was associated with a higher expression of RANKL and OPG. Various studies indicate that RANKL is the predominant stimulator of differentiation and proliferation of osteoclasts by binding RANK on the osteoclast cell membrane [42]. OPG, however, acts as decoy receptor for RANKL preventing RANKL-RANK binding, resulting in an inhibition of osteoclastogenesis [43,44]. Moreover, cartilage resorption and novel bone formation is associated with an elevated RANKL and OPG expression [45], whereas the pharmacological inhibition of RANKL leads to a delayed callus remodeling and fracture healing [46,47]. Finally, the higher osteoclast activity in cilostazol-treated mice may lead to an increased release of growth factors like transforming growth factor β1 (TGFβ1) and insulin-like growth factor 1 (IGF1). These growth factors induce the migration of mesenchymal stem cells to the bone surface and stimulate their differentiation towards the osteogenic lineage [48]. Hence, the elevated expression of RANKL and OPG as well as higher numbers of osteoclasts may have contributed to the improved bone regeneration by cilostazol treatment. Furthermore, there is accumulating evidence that the differentiation of osteoclasts is not only stimulated by RANKL, but also by VEGF. The binding of VEGF to VEGF-receptor(R)1 in monocytes

promotes their migration into the callus and their subsequent differentiation to osteoclasts [49,50]. Additionally, the binding of VEGF to VEGFR2 on osteoclasts itself promotes their survival by the stimulation of PI3K/Akt signaling [51]. Therefore, the increased number of osteoclasts in cilostazol-treated mice may also be directly caused by the enhanced expression of VEGF.

Bone injury induces an inflammatory response that is vital for successful healing and bone regeneration. A plethora of immune cells, most importantly macrophages, orchestrate and mediate inflammatory processes within the callus tissue. The inflammatory response triggers the vascularization of the callus tissue, subsequently providing the fracture site with vital nutrients, oxygen and osteoblastic cells [52]. Furthermore, macrophages can directly participate in bone regeneration by inducing the migration of mesenchymal stem cells to the callus, promoting osteoblast proliferation and differentiation as well as increasing collagen I deposition and stimulating matrix mineralization [52,53]. The major role of macrophages during fracture repair is highlighted by a recent experimental study by Schlundt et al. [54]. The authors demonstrated that the depletion of macrophages through clodronate liposomes significantly delays the process of endochondral ossification and callus formation [54]. Consequently, the increased number of macrophages in cilostazol-treated mice at 2 weeks after surgery may have directly contributed to the improved bone regeneration observed in the present study.

Taken together, our results demonstrate that cilostazol effectively stimulates vascularization and bone formation in atrophic non-unions, most likely by an upregulation of VEGF and by increasing the number of osteoclasts and macrophages within the callus tissue. In comparison to experimental pharmacological agents, which often lack reliable studies on potential side effects, cilostazol is an already approved drug that has been used in clinical practice for many years. Hence, cilostazol may represent a potent and safe compound for an adjuvant treatment of non-union formation.

CRediT authorship contribution statement

Maximilian M. Menger: Data analysis, Figure preparation, Data discussion and interpretation, Manuscript writing. **Michelle Bleimehl:** Surgery, Radiological, biomechanical and histological analysis. **David Bauer:** Surgery, Radiological analysis. **Claudia Scheuer:** Western blot analysis. **Sandra Hans:** Western blot and histological analysis. **Dominik Saul, Sabrina Ehnert**: Data discussion and interpretation, Critical manuscript revision. **Michael D. Menger, Tina Histing:** Idea and study design, Data interpretation, Manuscript writing. **Matthias W. Laschke:** Idea and study design, Data discussion and interpretation, Critical manuscript revision. All authors reviewed and approved the final version of the manuscript.

Declaration of Competing Interest

The authors have no relevant financial or non-financial interests to disclose. The authors have no conflicts of interest to declare that are relevant to the content of this article. All authors certify that they have no affiliations with or involvement in any organization or entity with any financial interest or non-financial interest in the subject matter or materials discussed in this manuscript. The authors have no financial or proprietary interests in any material discussed in this article.

Acknowledgements

We are grateful for the excellent technical assistance of Caroline Bickelmann and Julia Parakenings. The authors thank Servier Medical Art for providing access to designed medical elements (https:// smart.servier.com/), supporting the generation of graphical items in this publication.

References

1 T.A. Einhorn, L.C. Gerstenfeld, Fracture healing: mechanisms and interventions, Nat. Rev. Rheuma 11 (1) (2015) 45–54.
2 P. Garcia, et al., Temporal and spatial vascularization patterns of unions and nonunions: role of vascular endothelial growth factor and bone morphogenetic proteins, J. Bone Jt. Surg. Am. 94 (1) (2012) 49–58.
3 M.M. Menger, et al., Vascularization strategies in the prevention of non-union formation, Tissue Eng. Part B Rev. (2020).
4 D. Paley, et al., Ilizarov treatment of tibial nonunions with bone loss, Clin. Orthop. Relat. Res 241 (1989) 146–165.
5 B.G. Weber, C. Brunner, The treatment of nonunions without electrical stimulation, Clin. Orthop. Relat. Res 161 (1981) 24–32.
6 T.D. Fang, et al., Angiogenesis is required for successful bone induction during distraction osteogenesis, J. Bone Min. Res 20 (7) (2005) 1114–1124.
7 M. Murnaghan, G. Li, D.R. Marsh, Nonsteroidal anti-inflammatory drug-induced fracture nonunion: an inhibition of angiogenesis? J. Bone Jt. Surg. Am. 88 (Suppl 3) (2006) 140–147.
8 M. Fassbender, et al., Local inhibition of angiogenesis results in an atrophic non-union in a rat osteotomy model, Eur. Cell Mater. 22 (2011) 1–11.
9 T. Kamiya, S. Sakaguchi, Hemodynamic effects of the antithrombotic drug cilostazol in chronic arterial occlusion in the extremities, Arzneimittelforschung 35 (7A) (1985) 1201–1203.
10 Y. Liu, et al., Inhibition of adenosine uptake and augmentation of ischemia-induced increase of interstitial adenosine by cilostazol, an agent to treat intermittent claudication, J. Cardiovasc Pharm. 36 (3) (2000) 351–360.
11 J.H. Kim, et al., Combinatorial effect of probucol and cilostazol in focal ischemic mice with hypercholesterolemia, J. Pharm. Exp. Ther. 338 (2) (2011) 451–457.
12 T. Morikawa, et al., The effects of cilostazol on tissue oxygenation upon an ischemic-reperfusion injury in the mouse cerebrum, Adv. Exp. Med Biol. 662 (2010) 89–94.
13 W.R. Hiatt, Pharmacologic therapy for peripheral arterial disease and claudication, J. Vasc. Surg. 36 (6) (2002) 1283–1291.
14 F. Biscetti, et al., Cilostazol promotes angiogenesis after peripheral ischemia through a VEGF-dependent mechanism, Int J. Cardiol. 167 (3) (2013) 910–916.
15 S.Y. Tseng, et al., Effects of cilostazol on angiogenesis in diabetes through adiponectin/adiponectin receptors/sirtuin1 signaling pathway, Int J. Mol. Sci. 23 (2022) 23.
16 E. Paronis, et al., Cilostazol mediates immune responses and affects angiogenesis during the acute phase of hind limb ischemia in a mouse model, J. Cardiovasc Pharm. Ther. 25 (3) (2020) 273–285.
17 R. Li, et al., Effect of cell-based VEGF gene therapy on healing of a segmental bone defect, J. Orthop. Res 27 (1) (2009) 8–14.
18 H. Peng, et al., VEGF improves, whereas sFlt1 inhibits, BMP2-induced bone formation and bone healing through modulation of angiogenesis, J. Bone Min. Res 20 (11) (2005) 2017–2027.
19 T. Tsutsumimoto, et al., A phosphodiesterase inhibitor, pentoxifylline, enhances the bone morphogenetic protein-4 (BMP-4)-dependent differentiation of osteoprogenitor cells, Bone 31 (3) (2002) 396–401.
20 S. Wakabayashi, et al., Involvement of phosphodiesterase isozymes in osteoblastic differentiation, J. Bone Min. Res 17 (2) (2002) 249–256.
21 S.C. Herath, et al., Stimulation of angiogenesis by cilostazol accelerates fracture healing in mice, J. Orthop. Res 33 (12) (2015) 1880–1887.
22 M.M. Menger, et al., Establishment of a reliable model to study the failure of fracture healing in aged mice, J. Gerontol. A Biol. Sci. Med Sci. 77 (5) (2022) 909–917.
23 P. Garcia, et al., Development of a reliable non-union model in mice, J. Surg. Res 147 (1) (2008) 84–91.
24 T. Histing, et al., Ex vivo analysis of rotational stiffness of different osteosynthesis techniques in mouse femur fracture, J. Orthop. Res 27 (9) (2009) 1152–1156.
25 F.S. Frueh, et al., Short-term molecular and cellular effects of ischemia/reperfusion on vascularized lymph node flaps in rats, PLoS One 15 (10) (2020), e0239517.
26 S. Mallidi, et al., Prediction of tumor recurrence and therapy monitoring using ultrasound-guided photoacoustic imaging, Theranostics 5 (3) (2015) 289–301.
27 L.J. Rich, M. Seshadri, Photoacoustic imaging of vascular hemodynamics: validation with blood oxygenation level-dependent MR imaging, Radiology 275 (1) (2015) 110–118.
28 F.S. Frueh, et al., Prevascularization of dermal substitutes with adipose tissue-derived microvascular fragments enhances early skin grafting, Sci. Rep. 8 (1) (2018) 10977.
29 M.M. Menger, et al., Photoacoustic imaging for the study of oxygen saturation and total hemoglobin in bone healing and non-union formation, Photoacoustics 28 (2022), 100409.
30 P. Bosemark, et al., Augmentation of autologous bone graft by a combination of bone morphogenic protein and bisphosphonate increased both callus volume and strength, Acta Orthop. 84 (1) (2013) 106–111.
31 E.F. Morgan, et al., Micro-computed tomography assessment of fracture healing: relationships among callus structure, composition, and mechanical function, Bone 44 (2) (2009) 335–344.
32 L.C. Gerstenfeld, et al., Application of histomorphometric methods to the study of bone repair, J. Bone Min. Res 20 (10) (2005) 1715–1722.
33 M.M. Menger, et al., The vascularization paradox of non-union formation, Angiogenesis 25 (3) (2022) 279–290.
34 G. Victoria, et al., Bone stimulation for fracture healing: What's all the fuss? Indian J. Orthop. 43 (2) (2009) 117–120.
35 M.M. Menger, et al., Comparison of two non-union models with damaged periosteum in mice: Segmental defect and pin-clip fixation versus transverse fracture and K-wire stabilization, Bone 162 (2022), 116475.

36 P. Garcia, et al., Rodent animal models of delayed bone healing and non-union formation: a comprehensive review, Eur. Cell Mater. 26 (2013) 1–12.
37 J.M. Kanczler, R.O. Oreffo, Osteogenesis and angiogenesis: the potential for engineering bone, Eur. Cell Mater. 15 (2008) 100–114.
38 C.S. Bahney, et al., Cellular biology of fracture healing, J. Orthop. Res 37 (1) (2019) 35–50.
39 M.R. Hausman, M.B. Schaffler, R.J. Majeska, Prevention of fracture healing in rats by an inhibitor of angiogenesis, Bone 29 (6) (2001) 560–564.
40 B. Beamer, C. Hettrich, J. Lane, Vascular endothelial growth factor: an essential component of angiogenesis and fracture healing, HSS J. 6 (1) (2010) 85–94.
41 N.C. Keramaris, et al., Fracture vascularity and bone healing: a systematic review of the role of VEGF, Injury 39 (Suppl 2) (2008) S45–S57.
42 A. Leibbrandt, J.M. Penninger, RANKL/RANK as key factors for osteoclast development and bone loss in arthropathies, Adv. Exp. Med Biol. 649 (2009) 100–113.
43 D.L. Lacey, et al., Osteoprotegerin ligand is a cytokine that regulates osteoclast differentiation and activation, Cell 93 (2) (1998) 165–176.
44 W.S. Simonet, et al., Osteoprotegerin: a novel secreted protein involved in the regulation of bone density, Cell 89 (2) (1997) 309–319.
45 L.C. Gerstenfeld, et al., Comparison of effects of the bisphosphonate alendronate versus the RANKL inhibitor denosumab on murine fracture healing, J. Bone Min. Res 24 (2) (2009) 196–208.
46 T. Histing, et al., Pantoprazole, a proton pump inhibitor, delays fracture healing in mice, Calcif. Tissue Int 90 (6) (2012) 507–514.
47 T. Histing, et al., Melatonin impairs fracture healing by suppressing RANKL-mediated bone remodeling, J. Surg. Res 173 (1) (2012) 83–90.
48 J.F. Charles, A.O. Aliprantis, Osteoclasts: more than 'bone eaters', Trends Mol. Med 20 (8) (2014) 449–459.
49 B. Barleon, et al., Vascular endothelial growth factor up-regulates its receptor fms-like tyrosine kinase 1 (FLT-1) and a soluble variant of FLT-1 in human vascular endothelial cells, Cancer Res 57 (23) (1997) 5421–5425.
50 E. Zelzer, et al., Skeletal defects in VEGF(120/120) mice reveal multiple roles for VEGF in skeletogenesis, Development 129 (8) (2002) 1893–1904.
51 Q. Yang, et al., VEGF enhancement of osteoclast survival and bone resorption involves VEGF receptor-2 signaling and beta3-integrin, Matrix Biol. 27 (7) (2008) 589–599.
52 F. Loi, et al., Inflammation, fracture and bone repair, Bone 86 (2016) 119–130.
53 J. Loffler, et al., Compromised bone healing in aged rats is associated with impaired M2 macrophage function, Front Immunol. 10 (2019) 2443.
54 C. Schlundt, et al., Macrophages in bone fracture healing: Their essential role in endochondral ossification, Bone 106 (2018) 78–89.